

Helical Hyperbolic Propagation

Yarden Mazor¹, and Andrea Alù^{1,2,3,4*}

¹Department of Electrical and Computer Engineering, The University of Texas at Austin, Austin,
TX 78712, USA

²Photonics Initiative, Advanced Science Research Center, City University of New York, New
York, NY 10031, USA

³Physics Program, Graduate Center, City University of New York, New York, NY 10026, USA

⁴Department of Electrical Engineering, City College of New York, New York, NY 10031, USA

Highly confined surface waves present unique opportunities to enhance light interactions with localized emitters or molecules. Hyperbolic wave propagation is particularly interesting since it opens the opportunity to enhance the local density of states over broad bandwidths. So far, hyperbolic propagation has been mostly studied in planar structures, which facilitates the analysis but somehow limits the realm of possibilities. Here we show that hyperbolic propagation along cylindrical tubes opens pathways towards strong interaction with fields carrying optical angular momentum, tailored polarization and field asymmetries, valley-specific excitation and routing. In addition, we demonstrate that various parameter regimes enable strong spin/helicity – momentum locking.

1. Introduction

Propagation of surface waves along planar structures has been a vastly studied subject over time. In the past decade, this subject has seen increased interest in the context of plasmonics and the emergence of metasurfaces, which offer new opportunities to control and manipulate

electromagnetic fields. One family of applications includes crafting the surface response to an impinging wave. These include manipulating absorption and transmission [1,2], nonreciprocal reflection and transmission [3,4], polarization control [5], and lensing [6–8]. More relevant to the present work is the research unveiling new phenomena related to surface wave propagation over metasurfaces. Propagation of surface waves on impedance metasurfaces has been extensively studied [9–11], offering the possibility to greatly increase light-matter interaction due to the strong confinement. In turn, metasurfaces can also be used to better control and steer the surface wave fields. By considering additional degrees of freedom to the metasurface response, such as magnetic response and bianisotropy we can further tailor the overall propagation characteristics [12]. More exotic surface wave phenomena were discussed, such as hyperbolic metasurfaces [13–15] for highly confined guiding and Purcell enhancement, and nonreciprocal sector-way guiding [16]. Combined with modern nanofabrication techniques, graphene flexibility and tunability allows us to envision and implement these phenomena.

Surface waves guided along curved surfaces have been comparatively less studied. One classical geometry is based on perfectly conducting sheath helices [17,18] - perfectly conducting current only at a specific angle with respect to the cylinder axis. These structures support the propagation of high order, highly confined circular modes carrying optical angular momentum (OAM) of the form $e^{in\varphi}$, where a mode with specific n has asymmetric guiding properties. Upon the emergence of carbon nanotubes, a generalization of the sheath helix turned out to be a good model to describe their electrodynamic properties, both in standard [19] and helical configurations [20]. Cylindrical and spherical sheath metasurfaces have also been considered as candidates for cloaking [21–23] and engineering nanoparticle response [24]. Propagation in helical / spiral structures was also considered in linear arrays of plasmonic nanoparticles. In [25], high sensitivity to field polarization

was demonstrated, and in [26] magnetic bias was incorporated to demonstrate non-reciprocal one-way propagation. With the recent advances in manufacturing techniques, we can envision more complex cylindrical surfaces, which may allow us to further tailor the propagation and asymmetric manipulation of OAM carrying waves in optical transmission and communication [27,28]. Examples of these waves include vortex beams such as Laguerre-Gauss beams [29] (with many more examples in [30]). Another promising venue for spin specific excitation is valleytronics, utilizing the valley degree of freedom in transition metal dichalcogenides to achieve spin-specific excitons [31–33]. In the context of scattering, a preliminary synthesis process aimed at the control of scattered fields using cylindrical metasurfaces was presented in [34].

In this work, we introduce the concept of hyperbolic tubes, which support positive electrical conductivity at a specific angle, and negative conductivity in the perpendicular direction. Analogously to planar hyperbolic metasurfaces [14,15,35], these tubes can be realized as hyperbolic metasurfaces rolled into tubes along a specific angle, as shown in figure (1). They enable extreme asymmetry in wave propagation, and interact in highly asymmetric ways with OAM radiating sources, opening interesting opportunities for nanophotonics, plasmonics and specifically valleytronics to achieve highly directional excitation and control of optical signals and waves.

2. Geometry of the problem

The geometry under consideration is shown in figure (1). To intuitively describe the surface response, we may relate it to a planar impedance surface folded into a cylinder, where the cylinder axis makes an angle θ with the principal axes (red and blue lines) of the impedance tensor. We

assume the surrounding medium to be free-space. The $\hat{\mathbf{z}}$ components of the EM fields guided along the cylinder can be written as [36]

$$E_z = \begin{Bmatrix} A_n^i I_n(\tau r) \\ A_n^o K_n(\tau r) \end{Bmatrix} e^{-j\beta z} e^{jn\phi}, \quad H_z = \begin{Bmatrix} B_n^i I_n(\tau r) \\ B_n^o K_n(\tau r) \end{Bmatrix} e^{-j\beta z} e^{jn\phi}, \quad (1)$$

where A_n^i and B_n^i are the amplitudes of transverse-magnetic (TM) and transverse-electric (TE) mode inside the cylinder, and A_n^o , B_n^o outside the cylinder. For surface waves to be guided, $\beta^2 = k_0^2 + \tau^2 > k_0^2$, with $k_0 = \omega\sqrt{\varepsilon_0\mu_0}$ is the free-space wavenumber. The other field components are calculated from equation (1) using Maxwell's equations [18,35] (see [appendix 1](#)). The properties of the impedance surface are taken into account through the boundary conditions

$$\hat{\mathbf{r}} \times (\mathbf{H}^o - \mathbf{H}^i)_{r=a} = \frac{1}{2} \underline{\underline{\boldsymbol{\sigma}}}_s (\mathbf{E}_{\tan}^i + \mathbf{E}_{\tan}^o) + \frac{1}{2} \underline{\underline{\mathbf{a}}} (\mathbf{H}_{\tan}^i + \mathbf{H}_{\tan}^o), \quad (2)$$

$$-\hat{\mathbf{r}} \times (\mathbf{E}^o - \mathbf{E}^i) = \frac{1}{2} \underline{\underline{\boldsymbol{\sigma}}}_{ms} (\mathbf{H}_{\tan}^i + \mathbf{H}_{\tan}^o) + \frac{1}{2} \underline{\underline{\mathbf{b}}} (\mathbf{E}_{\tan}^i + \mathbf{E}_{\tan}^o). \quad (3)$$

Here, $\underline{\underline{\boldsymbol{\sigma}}}_s, \underline{\underline{\boldsymbol{\sigma}}}_{ms}$ are the electric and magnetic conductivity tensors, $\underline{\underline{\mathbf{a}}}, \underline{\underline{\mathbf{b}}}$ are the bianisotropic electric-magnetic coupling tensors, and the suffix *tan* stands for field components tangential to the cylinder surface ($\hat{\boldsymbol{\phi}}, \hat{\mathbf{z}}$). Assuming lossless, reciprocal and local surfaces renders $\underline{\underline{\boldsymbol{\sigma}}}_s, \underline{\underline{\boldsymbol{\sigma}}}_{ms}$ purely imaginary and symmetric and $\underline{\underline{\mathbf{a}}}, \underline{\underline{\mathbf{b}}}$ are real and satisfy $\underline{\underline{\mathbf{b}}} = -\underline{\underline{\mathbf{a}}}^T$ [5,38]. A preliminary analysis of surface wave propagation over isotropic uniaxial impedance tubes was derived in the context of carbon nanotubes in [19,20]. However, higher order modes were considered there for a specific case only that does not illuminate the phenomena we study in the following.

3. Asymmetric propagation over hyperbolic tubes

Surface wave propagation on hyperbolic metasurfaces have been shown to support many interesting phenomena, including broadband, highly confined surface waves, and enhanced local density of states. In the following, we show that the application of these properties in cylindrical tubes combines and couples them with orbital angular momentum, which can lead to valley selective propagation. We pay particular attention to hyperbolic surfaces folded along various directions, analyzing their guiding properties as the folding angle θ is changed, which is incorporated into the equations by properly rotating the surface matrices $\underline{\underline{\sigma}}_s, \underline{\underline{\sigma}}_{ms}, \underline{\underline{\mathbf{a}}}, \underline{\underline{\mathbf{b}}}$ (see [Appendix 1](#)). We start by considering surfaces with only a non-zero electric conductivity tensor of the form

$$\underline{\underline{\sigma}}_s = \frac{j}{\eta_0} \begin{pmatrix} X_1 & 0 \\ 0 & X_2 \end{pmatrix}. \quad (4)$$

In the special case of $X_1 = 0$, consistent with the geometry analyzed in [17,18], the dispersion equation becomes

$$\frac{I_n'(\tau a) K_n'(\tau a)}{I_n(\tau a) K_n(\tau a)} = -\frac{(n\beta a + a^2 \tau^2 \cot \theta)^2}{k_0^2 a^4 \tau^2} - \frac{1 + \cot^2 \theta}{k_0 a X_2 I_n(\tau a) K_n(\tau a)}, \quad (5)$$

Which collapses to the relation presented in [17,18] when $X_2 \rightarrow \infty$. I_n', K_n' are the first derivatives of the modified Bessel functions with respect to the argument [37]. A dispersion plot

is shown in figure (2a) for $\theta = \pi/4$, $X_2 = -4$ and since we have chosen an inductive surface with $X_2 < 0$, the modes are quasi-TM in nature. We see an interesting chiral asymmetry in the band diagram, with positive and negative values of angular momentum n for opposite propagation directions [17,18], as expected based on time-reversal symmetry considerations. Each higher-order mode is shifted horizontally by $\Delta\beta = k_0 \tan \theta$. This case is a platform for interesting directional effects when such a waveguide interacts with a wave carrying angular momentum due to the asymmetry present.

This asymmetry can be pushed further if we add a hyperbolic response to the surface, considering $X_1 > 0$. In [Appendix 2](#) we give some of the guiding characteristics for a general relation between X_1 and X_2 , where here, for simplicity, we will focus on the special case $|X_1| = |X_2| = X$, for skew angle of $\theta = 45^\circ$. The dispersion equation in this scenario becomes

$$\frac{1}{\tau a} - \tau a I_n K_n I_n' K_n' + \frac{2\beta n X}{\tau a} I_n K_n = 0, \quad (6)$$

and the corresponding dispersion curves are shown in figure (2b) for $X_2 = -X = -4$. The asymmetry with respect to the mode index is more extreme here, and positive angular-momentum modes can propagate only to the right, whereas negative angular-momentum propagates to the left. This OAM-momentum coupling is reminiscent of the edge state spin-momentum coupling in photonic topological insulators [39]. The zero-index mode ($n = 0$) is not supported at all, making the waveguide completely dark to OAM neutral excitation. Each mode has a horizontal asymptote (red dashed lines in Fig. (2b)) at (calculation remarks in [Appendix 3](#))

$$\frac{2\pi f_{r,n}a}{c} = \frac{4|nX|}{4+X^2}, \quad (7)$$

corresponding to surface waves highly confined to the tube. In this scenario, the modes have balanced TM and TE nature, implying that they can strongly interact with a wide range of polarizations, with an ideal optical response to sort angular momentum and valley responses. Operating close to $f_{r,n}$, we expect highly mode-selective operation, due to the significant differences in mode confinement, and cutoff of the lower modes. To examine these opportunities, we consider two nearby localized emitters with same magnitude polarized along $\hat{\mathbf{z}}$, but with different phase, positioned in the location of the green vectors in figure (2c,2d). Such a source is used as a simple version of an excitation that couples efficiently to a specific value of orbital angular momentum n . Naturally, a mode n would best couple to a current source of the form $J_z = J_{z0}e^{in\phi}$. Our two-dipole source is just a 2-point sampling of this optimal current distribution. The phase difference is chosen to couple to the $n=3$ mode, and the excitation frequency is $0.985f_{r,3}$. When the emitters excite the helical tube of figure (2a), many modes are excited (the insets show the relative intensity of each mode n), and no directionality is obtained. Figure (2d) shows the same excitation when applied to the hyperbolic helical tube, displaying highly mode-selective propagation and directionality. This can allow us to design emitters that strongly couple and launch specific angular momentum values using finite tube sections. Additional insights can be gained by examining the optical helicity density \mathfrak{S} [40,41] for the modes supported by the hyperbolic tube, as calculated in [Appendix 3](#). Since our interest is focused on the highly confined modes, this calculation can be greatly simplified by examining $\mathfrak{S}_\infty = \mathfrak{S}(\beta \gg k_0)$. In particular, it follows that $\text{sign}(\mathfrak{S}_\infty^{i,o}) = \pm \text{sign}(X)$. This can help customize the way our waveguide interacts

with spin and helicity carrying sources such as valley excitons. In particular, one can envision directional sorting and routing of valley excitons using the aforementioned interactions when hyperbolic tubes are coated with excitonic layers around the resonant frequencies of the various modes.

4. Asymmetry enhancement using magnetic response

By virtue of duality, hyperbolic magnetic tubes, characterized by only magnetic conductivity in (4), will present dual propagation features to the case analyzed in figure (2). Interesting opportunities arise if we combine these two responses, further enhancing the asymmetry and directionality of the supported modes. As a testbed, we examine the case of a planar surface with

$$\underline{\underline{\sigma}}_s = \frac{j}{\eta_0} \begin{pmatrix} X & 0 \\ 0 & -X \end{pmatrix}, \underline{\underline{\sigma}}_{ms} = j\eta_0 \begin{pmatrix} X_m & 0 \\ 0 & -X_m \end{pmatrix}, \mathbf{a} = \mathbf{b} = \begin{pmatrix} 0 & \Omega \\ -\Omega & 0 \end{pmatrix}. \quad (8)$$

Using a *balanced* surface, satisfying $X_m = X$, and combining it with a properly tailored value of Ω , the modal asymmetry manifests through an interestingly one-sided field distribution of the propagating fields, as shown in figure (3a). The Ω response is required to tailor the cross-interaction between the electric and magnetic fields, which gives rise to this field asymmetry. High order guided cylindrical modes contain an inherent and rich coupling between electric and magnetic fields, allowing us to achieve similar asymmetries without the need for an Ω -type response. Let us examine an electric-magnetic surface described by $\underline{\underline{\sigma}}_s, \underline{\underline{\sigma}}_{ms}$ from equation (8), satisfying $\mathbf{a} = \mathbf{b} = 0$, and folded into a cylinder, with $\theta = 45^\circ$. We find two types of solutions for each mode index n , corresponding to two distinct dispersion branches. The dispersion equations are

$$8nX\beta I_n K_n + \tau a \left[(X \mp 2)^2 I_n' K_n - (X \pm 2)^2 I_n K_n' \right] = 0, \quad (9)$$

where the upper and lower signs correspond to two distinct solution families. The dispersion curves are shown in figure (3b), and the modal fields satisfy

$$E_z^{i,o}(r=a) = \pm j\eta_0 H_z^{i,o}(r=a), \quad (10)$$

as long as the surface is balanced, and regardless of X , where the plus (minus) sign corresponds to the two distinct modal solutions. When substituting the dispersion solutions back into the governing equations (20) to obtain the mode profile, the difference between the two modal solutions becomes apparent. The field amplitudes on the tube surface (both electric and magnetic, according to equation (10)) satisfy

$$\frac{|E_z^i|}{|E_z^o|} = \frac{|H_z^i|}{|H_z^o|} = \frac{(X \pm 2)}{(X \mp 2)} \quad (11)$$

Yielding that the first set of modes is concentrated mostly in the outer side, while the second is on the inner region, corresponding to the labels in Figure (3b). This figure also shows that, by tuning the operation frequency to be slightly above or below $f_{r,n}$, we can control which mode is dominant. When $X = 2$, we maximize the contrast between inside and outside fields, yielding slow-wave modes concentrated purely in the interior or exterior part of the cylinder. In this extreme scenario, the modes not only spatially separated, but also totally spectrally separated – they are guided in completely different frequency bands, as shown in figure (3c). New cutoff frequencies at $k_{0,c}a = \sqrt{n(n+1)}$ are induced in this regime (blue lines in the figure). In this scenario, Eq. (10)

ensures that $\text{sign}(\mathfrak{S}_\infty) = \mp 1$, coupling the helicity to the geometrical domain where the fields are concentrated.

Another interesting class, is the *conjugate* tubes, corresponding to $X_m = -4/X$. Here, the “folded” surface has both electric and magnetic hyperbolicity, but in complementary directions, and as before we perform the folding along the $\theta = 45^\circ$ line. The dispersion equation obtained in this case is completely symmetric for propagation to the left and right directions

$$|n\beta| = \frac{(k_0 a)(\tau a)}{4|X|} \sqrt{\left(4 \frac{K'_n}{K_n} - \frac{I'_n}{I_n} X^2\right) \left(\frac{K'_n}{K_n} X^2 - 4 \frac{I'_n}{I_n}\right)} \quad (12)$$

And the curves obtained are shown in figure (4) for $X = 4$. The asymmetry in this case is revealed when closely examining the helicity of the propagating modes, satisfying $\text{sign}(\mathfrak{S}_\infty^{i,o}) = -\text{sign}(n\beta)$ and exhibiting strong helicity-momentum-OAM coupling. Additionally, it is worth mentioning the case of $X_m = -X$. Here, no such pronounced asymmetry is present, however it allows tailoring of the TE/TM ratio of the propagating waves. If we denote this ratio ζ (same notation is also used in [Appendix 3](#)) we obtain

$$|\zeta| = \frac{|E_z|}{|\eta_0 H_z|} = \left| \frac{X}{2} \right| \quad (13)$$

with dispersion curve very similar to the previous case.

5. Conclusions

In this paper, we have explored surface wave propagation over hyperbolic tubes, showing that they can form an interesting platform for nanophotonics and valleytronics applications. They yield

highly asymmetric propagation properties in terms of angular momentum, enabling largely unusual responses when properly tuning their impedance parameters. Around the resonance frequencies, the structures obtained strongly interact with OAM carrying waves such as vortex beams and valley excitons. These tubes also give rise to tunable asymmetry in terms of propagating fields when adding into the picture electric and magnetic hyperbolicity, such as high field contrast between the inner and outer domains in addition to the asymmetric propagation. For all of the cases studied, strong OAM-momentum coupling was demonstrated which can be viewed as an extension of the spin-momentum coupling present in topological edge states. For each studied case, it was shown that the sign of the optical helicity for the propagating waves is controlled and coupled to various parameters – surface conductivity, field propagation domain, OAM and wavenumber.

Appendix 1

To obtain the dispersion equation, we start by expressing the tangent fields using the coefficients

A^i, A^o, B^i, B^o defined in equation (1), arranged in a vector $\mathbf{C}^{i,o} = (A^{i,o}, B^{i,o})^T$

$$\mathbf{E}^{i,o} = e^{jn\varphi} e^{-j\beta z} \underline{\underline{\mathbf{M}}}_{E,(i,o)} \mathbf{C}^{i,o}, \quad \mathbf{H}^{i,o} = e^{jn\varphi} e^{-j\beta z} \underline{\underline{\mathbf{M}}}_{H,(i,o)} \mathbf{C}^{i,o} \quad (14)$$

and the matrices $\underline{\underline{\mathbf{M}}}_E, \underline{\underline{\mathbf{M}}}_H$ are defined as [18,36]

$$\mathbf{E}_{n,\tan}^i(r=a) = \begin{bmatrix} E_\varphi^i \\ E_z^i \end{bmatrix}_{r=a} = e^{jn\varphi-j\beta z} \begin{bmatrix} -\frac{n\beta}{\tau^2} I_n(\tau a) & -\frac{jk_0 a}{\tau} I_n'(\tau a) \\ I_n(\tau a) & 0 \end{bmatrix} \begin{bmatrix} A_n^i \\ B_n^i \end{bmatrix} = e^{jn\varphi-j\beta z} \underline{\underline{\mathbf{M}}}_{E,i} \mathbf{C}^i, \quad (15)$$

$$\mathbf{E}_{n,\tan}^o(r=a) = \begin{bmatrix} E_\varphi^o \\ E_z^o \end{bmatrix}_{r=a} = e^{jn\varphi-j\beta z} \begin{bmatrix} -\frac{n\beta}{\tau^2} K_n(\tau a) & -\frac{jk_0 a}{\tau} K_n'(\tau a) \\ K_n(\tau a) & 0 \end{bmatrix} \begin{bmatrix} A_n^o \\ B_n^o \end{bmatrix} = e^{jn\varphi-j\beta z} \underline{\underline{\mathbf{M}}}_{E,o} \mathbf{C}^o, \quad (16)$$

$$\mathbf{H}_{n,\tan}^i(r=a) = \begin{bmatrix} H_\varphi^i \\ H_z^i \end{bmatrix}_{r=a} = e^{jn\varphi - j\beta z} \begin{bmatrix} \frac{jk_0 a}{\tau} I_n'(\tau a) & -\frac{n\beta}{\tau^2} I_n(\tau a) \\ 0 & I_n(\tau a) \end{bmatrix} \begin{bmatrix} A_n^i \\ B_n^i \end{bmatrix} = e^{jn\varphi - j\beta z} \underline{\underline{\mathbf{M}}}_{H,i} \mathbf{C}^i, \quad (17)$$

$$\mathbf{H}_{n,\tan}^o(r=a) = \begin{bmatrix} H_\varphi^o \\ H_z^o \end{bmatrix}_{r=a} = e^{jn\varphi - j\beta z} \begin{bmatrix} \frac{jk_0 a}{\tau} K_n'(\tau a) & -\frac{n\beta}{\tau^2} K_n(\tau a) \\ 0 & K_n(\tau a) \end{bmatrix} \begin{bmatrix} A_n^o \\ B_n^o \end{bmatrix} = e^{jn\varphi - j\beta z} \underline{\underline{\mathbf{M}}}_{H,o} \mathbf{C}^o. \quad (18)$$

In addition, we represent the $\hat{\mathbf{r}} \times$ operation using a 2×2 matrix $\hat{\mathbf{r}} \times \mathbf{V}_{\tan} = \mathbf{N}_r \mathbf{V}_{\tan}$. We also define

the unitless conductivity matrices $\underline{\underline{\mathbf{X}}}_s, \underline{\underline{\mathbf{X}}}_{ms}$

$$\underline{\underline{\boldsymbol{\sigma}}}_s = j \underline{\underline{\mathbf{X}}}_s / \eta_0, \quad \underline{\underline{\boldsymbol{\sigma}}}_{ms} = j \underline{\underline{\mathbf{X}}}_{ms} \eta_0. \quad (19)$$

To express the skewed boundary conditions, we rotate each of the fields by the angle θ with respect to $\hat{\mathbf{z}}$, and then rotate the result back to the lab frame. This results in rotated conductivity matrices of the form $\underline{\underline{\mathbf{m}}}^\theta = \underline{\underline{\mathbf{R}}}^\theta \underline{\underline{\mathbf{m}}} \underline{\underline{\mathbf{R}}}^{-\theta}$, where $\underline{\underline{\mathbf{m}}}$ is any of tensors defined in the constitutive relations in equations (2) and (3), and $\underline{\underline{\mathbf{R}}}^\theta$ is the 2D rotation matrix by angle θ . By substituting these into the boundary conditions in equations (2) and (3) we obtain

$$\underline{\underline{\mathbf{M}}} \mathbf{C} = \begin{bmatrix} \frac{1}{2} \underline{\underline{\mathbf{X}}}_s^\theta \underline{\underline{\mathbf{M}}}_{E,i} + \left(\frac{1}{2} \underline{\underline{\mathbf{a}}}^\theta + \underline{\underline{\mathbf{N}}}_r \right) \underline{\underline{\mathbf{M}}}_{H,i} & \frac{1}{2} \underline{\underline{\mathbf{X}}}_s^\theta \underline{\underline{\mathbf{M}}}_{E,o} + \left(\frac{1}{2} \underline{\underline{\mathbf{a}}}^\theta - \underline{\underline{\mathbf{N}}}_r \right) \underline{\underline{\mathbf{M}}}_{H,o} \\ \left(\frac{1}{2} \underline{\underline{\mathbf{b}}}^\theta - \underline{\underline{\mathbf{N}}}_r \right) \underline{\underline{\mathbf{M}}}_{E,i} + \frac{1}{2} \underline{\underline{\mathbf{X}}}_{ms}^\theta \underline{\underline{\mathbf{M}}}_{H,i} & \left(\frac{1}{2} \underline{\underline{\mathbf{b}}}^\theta + \underline{\underline{\mathbf{N}}}_r \right) \underline{\underline{\mathbf{M}}}_{E,o} + \frac{1}{2} \underline{\underline{\mathbf{X}}}_{ms}^\theta \underline{\underline{\mathbf{M}}}_{H,o} \end{bmatrix} \begin{bmatrix} \mathbf{C}^i \\ \mathbf{C}^o \end{bmatrix} = 0. \quad (20)$$

For a non-trivial solution to exist, we need $\text{Det}\{\underline{\underline{\mathbf{M}}}\} = 0$, providing the dispersion equation for propagating waves.

Appendix 2

For convenience, let us start by defining $X_2 = X, X_1 = -sX$ to describe a general hyperbolic tube.

The critical skew angle θ_c which gives the same type of responses seen for the simpler cases correspond to the condition that the zz component of the rotated conductivity tensor zero. This angle satisfies

$$\theta_c = \text{arccot} \left[\sqrt{s} \right]. \quad (21)$$

After some long, but straightforward algebra we obtain the dispersion equation

$$2nX\beta a\sqrt{s}I_nK_n + k_0a\left(1 - sX^2\tau^2a^2I_n'I_n'K_nK_n'\right) + \frac{X(1-s)}{\tau^2a^2}\left(n^2\beta^2a^2I_nK_n + k_0^2a^4\tau^2I_n'K_n'\right) = 0 \quad (22)$$

And if we substitute $s=1$ we will obtain equation (6). The series of resonance frequencies for each mode index n can be written in a similar way to equation (7)

$$\frac{2\pi f_{r,n}a}{c} = \frac{4\sqrt{s}|nX|}{4 + sX^2} \quad (23)$$

And a typical form of the dispersion is shown in figure (5) for two cases. The expressions for the resonance frequencies are obtained using the large argument approximated forms for the modified Bessel functions in the dispersion equations [42]. In both cases presented in figure (5), the values were chosen in a way that the off-diagonal terms in the rotated conductivity tensor defined in equation (4) of the main text will be the same. The difference, therefore, stems from the fact that in the general case the diagonal terms are not zero, and their value and sign determine the behavior of the additional dispersion branches.

Appendix 3

We use the helicity density definition from [40,41], which reads for our case

$$\mathfrak{S} = \frac{1}{2\omega} \text{Im}\{\mathbf{H}^* \cdot \mathbf{E}\} \quad (24)$$

In addition, for all cases examined in the main text, the relation between the TE and TM components can be characterized by

$$\eta_0 B_n^{i,o} = j \zeta_{i,o} A_n^{i,o} \quad (25)$$

with $\zeta \in \mathbb{R}$. This lets us write the helicity density of the guided fields as

$$\begin{aligned} \mathfrak{S}^i &= -\frac{|A_n^i|^2}{2\omega \bar{\tau}^4} \left[\zeta_i I_n^2(\bar{\tau}) \left[\bar{\tau}^4 + n^2 (\bar{\beta}^2 + \bar{a}^2) \right] + \zeta_i I_n'^2(\bar{\tau}) \bar{\tau}^2 (\bar{\beta}^2 + \bar{a}^2) - 2 I_n' I_n n \bar{\beta} \bar{\tau} \bar{a} (1 + \zeta_i^2) \right] \\ \mathfrak{S}^o &= -\frac{|A_n^o|^2}{2\omega \bar{\tau}^4} \left[\zeta_i K_n^2(\bar{\tau}) \left[\bar{\tau}^4 + n^2 (\bar{\beta}^2 + \bar{a}^2) \right] + \zeta_i K_n'^2(\bar{\tau}) \bar{\tau}^2 (\bar{\beta}^2 + \bar{a}^2) - 2 K_n' K_n n \bar{\beta} \bar{\tau} \bar{a} (1 + \zeta_i^2) \right] \end{aligned} \quad (26)$$

with $\bar{\beta} = \beta a$, $\bar{\tau} = \tau a$, $\bar{a} = k_0 a$. However, since in our work we study the highly confined waves, with large wave numbers, we can simplify this expression significantly

$$\begin{aligned} \mathfrak{S}_\infty^i &= -\frac{|A_n^i|^2 \zeta_i}{2\omega} \left[I_n^2(\bar{\tau}) + I_n'^2(\bar{\tau}) \right] \\ \mathfrak{S}_\infty^o &= -\frac{|A_n^i|^2 \zeta_i}{2\omega} \left[K_n^2(\bar{\tau}) + K_n'^2(\bar{\tau}) \right] \end{aligned} \quad (27)$$

where we used the symbol $\mathfrak{S}_\infty = \mathfrak{S}(\beta \gg k_0)$. This result is valid as long as ζ is not strongly dependent on $\bar{\beta}$, which is indeed the case in all of the systems examined. It is important to note

that for any value of $\bar{\tau}$ the expressions in the square brackets are positive, therefore, the sign of the helicity density is determined solely by the sign of ζ , and satisfies

$$\text{sign}(\mathfrak{S}_{\infty}^{i,o}) = -\text{sign}(\zeta^{i,o}) \quad (28)$$

References

- [1] V. S. Asadchy, I. A. Faniayeu, Y. Ra'di, S. A. Khakhomov, I. V. Semchenko, and S. A. Tretyakov, Phys. Rev. X **5**, 031005 (2015).
- [2] Y. Ra'di, C. R. Simovski, and S. A. Tretyakov, Phys. Rev. Appl. **3**, 037001 (2015).
- [3] Y. Hadad, A. R. Davoyan, N. Engheta, and B. Z. Steinberg, ACS Photonics **1**, 1068 (2014).
- [4] Y. Hadad, D. L. Sounas, and A. Alu, Phys. Rev. B - Condens. Matter Mater. Phys. **92**, 100304(R) (2015).
- [5] C. Pfeiffer and A. Grbic, Phys. Rev. Appl. **2**, 044011 (2014).
- [6] E. Forati, G. W. Hanson, A. B. Yakovlev, and A. Alù, Phys. Rev. B - Condens. Matter Mater. Phys. **89**, 081410(R) (2014).
- [7] M. Khorasaninejad, W. T. Chen, R. C. Devlin, J. Oh, A. Y. Zhu, and F. Capasso, Science (80-.). **352**, 1190 (2016).
- [8] N. Yu and F. Capasso, Nat. Mater. **13**, 139 (2014).
- [9] H. J. Bilow, IEEE Trans. Antennas Propag. **51**, 2788 (2003).
- [10] C. L. Holloway, D. C. Love, E. F. Kuester, J. A. Gordon, and D. A. Hill, IEEE Trans.

- Antennas Propag. **60**, 5173 (2012).
- [11] C. L. Holloway, E. F. Kuester, J. A. Gordon, J. O'Hara, J. Booth, and D. R. Smith, IEEE Antennas Propag. Mag. **54**, 10 (2012).
- [12] A. Epstein and G. V. Eleftheriades, IEEE Trans. Antennas Propag. **64**, 3880 (2016).
- [13] J. S. Gomez-Diaz, M. Tymchenko, and A. Alù, Phys. Rev. Lett. **114**, (2015).
- [14] J. S. Gomez-Diaz, M. Tymchenko, and A. Alù, Opt. Mater. Express **5**, 2313 (2015).
- [15] J. S. Gomez-Diaz and A. Alù, ACS Photonics **3**, 2211 (2016).
- [16] Y. Mazor and B. Z. Steinberg, Phys. Rev. Lett. **112**, 153901 (2014).
- [17] J. R. Pierce and P. K. Tien, Proc. IRE **42**, 1389 (1954).
- [18] D. A. Watkins, *Topics in Electromagnetic Theory* (John Wiley & Sons, New York, 1958).
- [19] G. Y. Slepyan, S. A. Maksimenko, and A. Lakhtakia, Phys. Rev. B - Condens. Matter Mater. Phys. **57**, 9485 (1998).
- [20] S. A. Maksimenko and G. Y. Slepyan, J. Commun. Technol. Electron. **47**, 235 (2002).
- [21] P. Y. Chen and A. Alù, Phys. Rev. B - Condens. Matter Mater. Phys. **84**, 205110 (2011).
- [22] T. Bian, X. Gao, S. Yu, L. Jiang, J. Lu, and P. T. Leung, Optik (Stuttg). **136**, 215 (2017).
- [23] T. Christensen, A. P. Jauho, M. Wubs, and N. A. Mortensen, Phys. Rev. B - Condens. Matter Mater. Phys. **91**, 125414 (2015).

- [24] B. K. Ari Sihvola, Dimitrios C. Tzarouchis, Pasi Ylä-Oijala, Henrik Wallén, ArXiv.Org 1805.09159 (2018).
- [25] D. Van Orden, Y. Fainman, and V. Lomakin, *Opt. Lett.* **35**, 2579 (2010).
- [26] Y. Hadad and B. Z. Steinberg, *Phys. Rev. Lett.* **105**, 233904 (2010).
- [27] J. Wang, J. Y. Yang, I. M. Fazal, N. Ahmed, Y. Yan, H. Huang, Y. Ren, Y. Yue, S. Dolinar, M. Tur, and A. E. Willner, *Nat. Photonics* **6**, 488 (2012).
- [28] A. E. Willner, H. Huang, Y. Yan, Y. Ren, N. Ahmed, G. Xie, C. Bao, L. Li, Y. Cao, Z. Zhao, J. Wang, M. P. J. Lavery, M. Tur, S. Ramachandran, A. F. Molisch, N. Ashrafi, and S. Ashrafi, *Adv. Opt. Photonics* **7**, 66 (2015).
- [29] L. Allen, M. W. Beijersbergen, R. J. C. Spreeuw, and J. P. Woerdman, *Phys. Rev. A* **45**, 8185 (1992).
- [30] M. J. Padgett, *Opt. Express* **25**, 11265 (2017).
- [31] K. F. Mak, K. He, J. Shan, and T. F. Heinz, *Nat. Nanotechnol.* **7**, 494 (2012).
- [32] A. Krasnok, S. Lepeshov, and A. Alú, *Opt. Express* **26**, 15972 (2018).
- [33] J. R. Schaibley, H. Yu, G. Clark, P. Rivera, J. S. Ross, K. L. Seyler, W. Yao, and X. Xu, *Nat. Rev. Mater.* **1**, 16055 (2016).
- [34] M. Safari, A. Abdolali, H. Kazemi, M. Albooyeh, M. Veysi, and F. Capolino, in *2017 IEEE Antennas Propag. Soc. Int. Symp. Proc.* (2017), pp. 1499–1500.
- [35] J. S. Gomez-Diaz, M. Tymchenko, and A. Alù, *Phys. Rev. Lett.* **114**, 233901 (2015).

- [36] D. Pozar, *Microwave Engineering Fourth Edition* (2005).
- [37] Throughout this work, the argument inside the modified Bessel functions and their derivatives is always τa , therefore we will omit this argument for brevity.
- [38] Jin Au Kong, Proc. IEEE **60**, 1036 (1972).
- [39] A. B. Khanikaev, S. H. Mousavi, W.-K. Tse, M. Kargarian, A. H. MacDonald, and G. Shvets, Nat. Mater. **12**, 233 (2013).
- [40] F. Alpeggiani, K. Y. Bliokh, F. Nori, and L. Kuipers, Phys. Rev. Lett. **120**, 243605 (2018).
- [41] K. Y. Bliokh, Y. S. Kivshar, and F. Nori, Phys. Rev. Lett. **113**, 033601 (2014).
- [42] F. W. J. Olver, D. W. Lozier, R. F. Boisvert, and C. W. Clark, *NIST Handbook of Mathematical Functions* (2010).

Figures

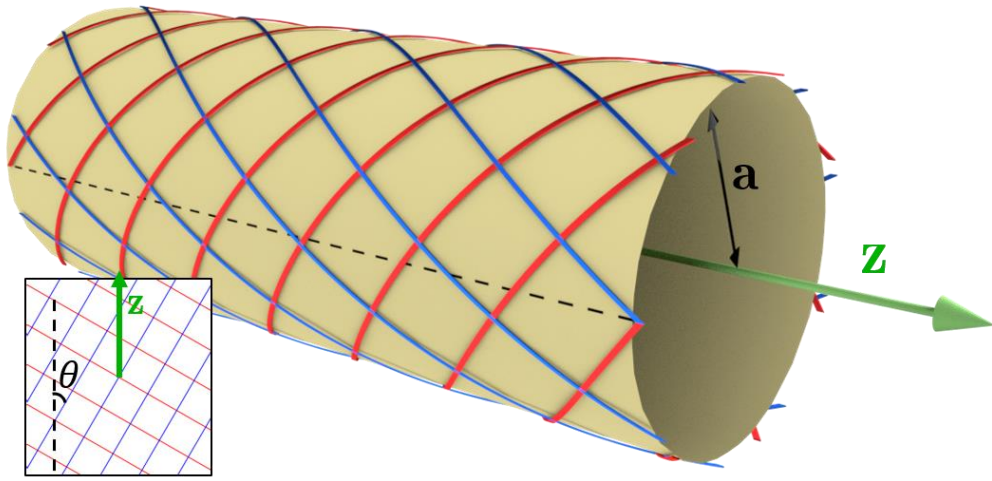


Figure 1. The geometry under analysis, showing the principal axes of the conductivity tensor. When rotated, they form a skewed reference system over the surface of the cylinder.

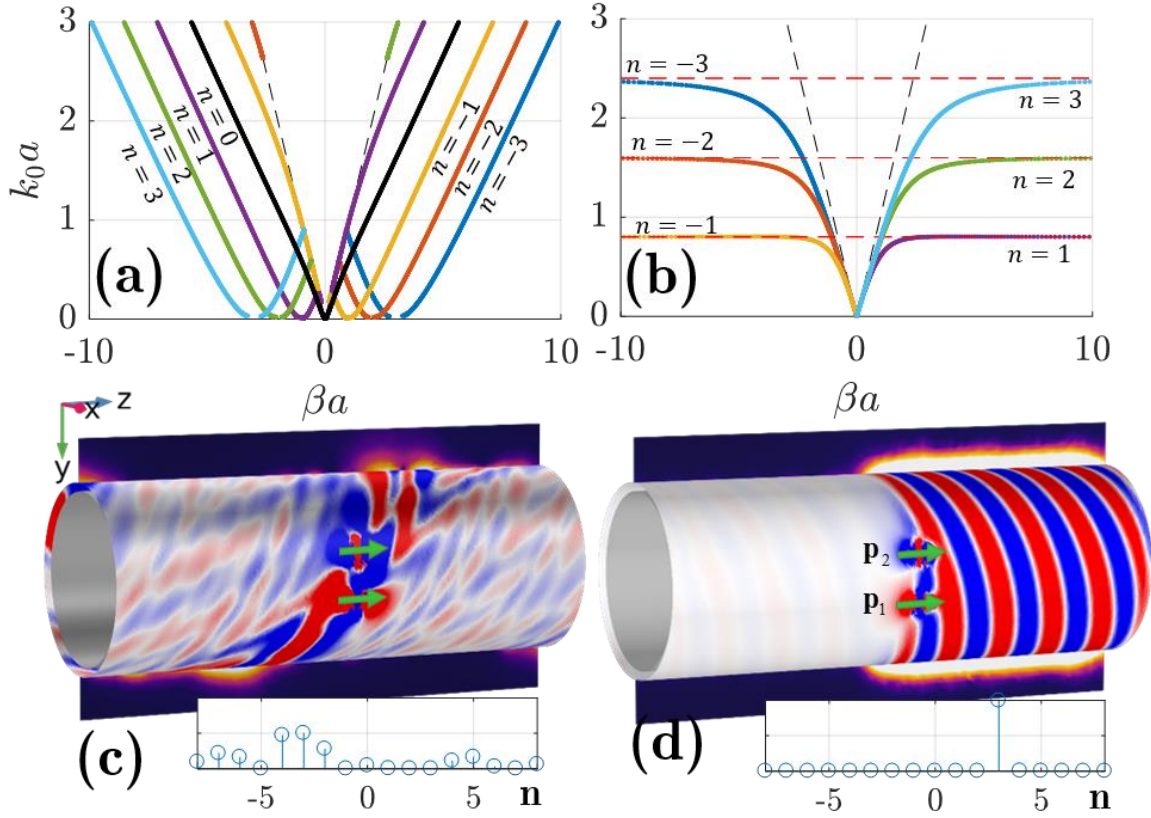


Figure 2. (a) Dispersion curves when only $\sigma_{s,zz}$ is present and $\theta = \pi/4$. Dashed black lines show the light-lines. (b) Relation between \hat{z} components of the EM field for the $n = \pm 2$ modes, for the case described in panel (a). (c) Dispersion curves for a “folded” hyperbolic surface (hyperbolic tube). Dashed black lines shown the light-lines. The mode $n = 0$ is not present, as it does not propagate. (d) same as (b) but for the hyperbolic tube case. (e) Wave numbers vs. the helical skew angle for the hyperbolic tube.

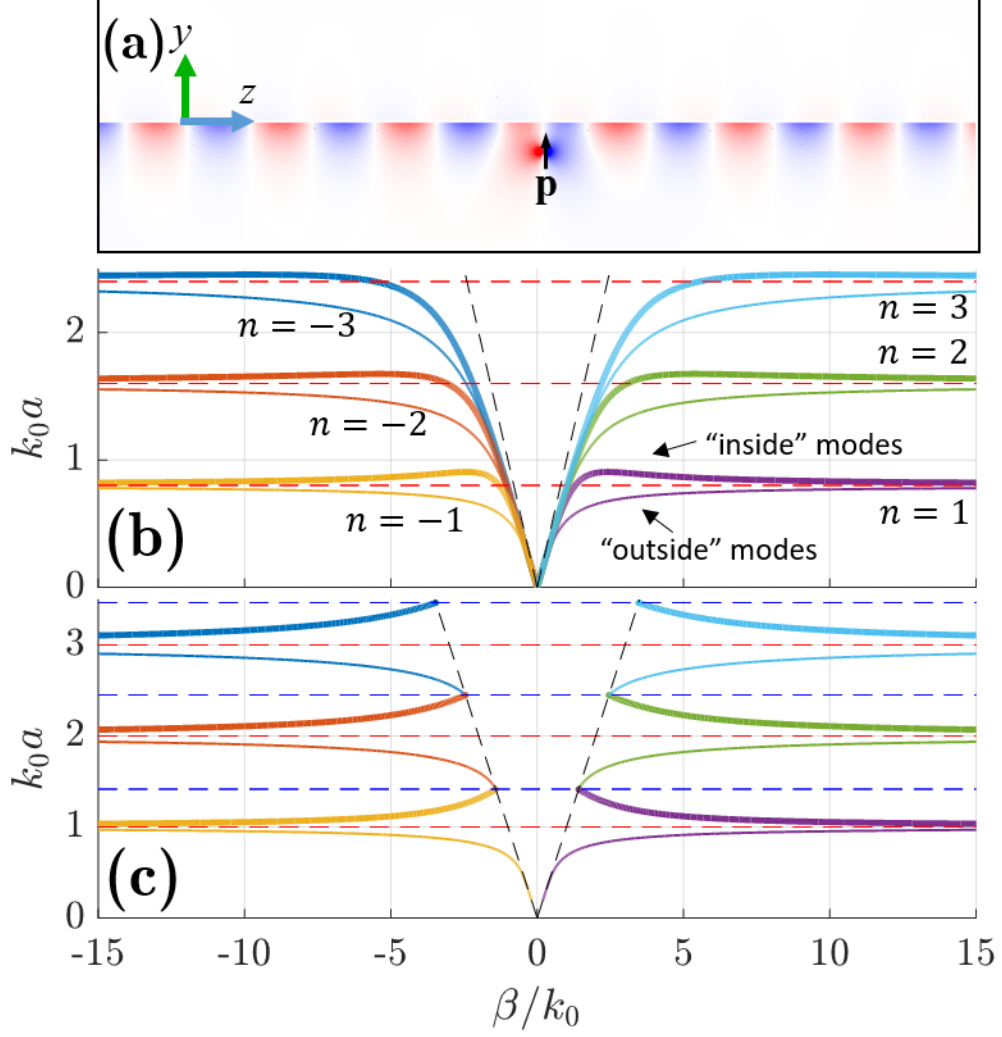


Figure 3. (a) Excitation of surface waves over a planar surface with balanced electric and magnetic hyperbolic dispersion. The modal fields are concentrated at the bottom surface (b) Dispersion curves for balanced tubes for $X = X_m = 4$. (c) Dispersion curves for the balanced tubes for $X = X_m = 2$.

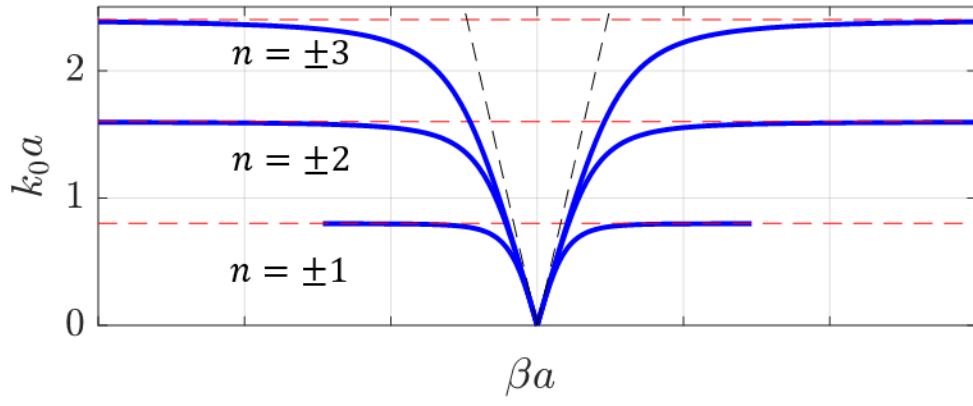


Figure 4. Dispersion curves of the conjugate cylinder, for $X = 4, X_m = -1$.

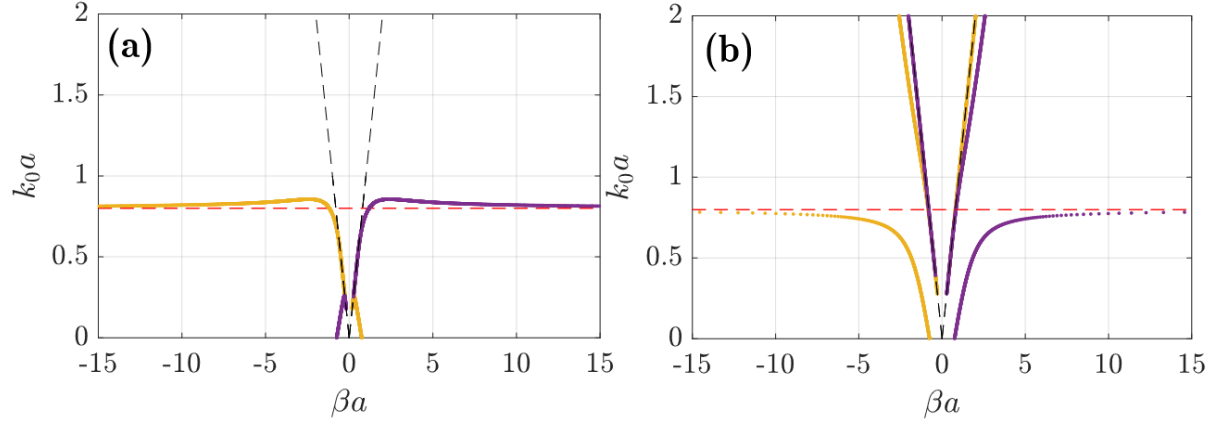


Figure 5. (a) Dispersion for a general hyperbolic electric tube for $\theta = \theta_c$, with $s = 0.25$, $X = -2$. Red dashed line shows the value of $k_0 a$ corresponding to $f_{c,1}$. (b) $s = 4$, $X = -0.5$.